Automated pericardium delineation and epicardial fat volume quantification from noncontrast CT

Xiaowei Ding[a)]
Biomedical Imaging Research Institute, Department of Biomedical Sciences, Cedars Sinai Medical Center, Los Angeles, California 90048 and Computer Science Department, Henry Samueli School of Engineering and Applied Science at UCLA, Los Angeles, California 90095

Demetri Terzopoulos[b)]
Computer Science Department, Henry Samueli School of Engineering and Applied Science at UCLA, Los Angeles, California 90095

Mariana Diaz-Zamudio[c)]
Nuclear Medicine Department, Cedars Sinai Medical Center, Los Angeles, California 90048

Daniel S. Berman[d)] and Piotr J. Slomka[e)]
Departments of Imaging and Medicine, Cedars Sinai Medical Center, Los Angeles, California 90048 and Department of Medicine, David-Geffen School of Medicine at UCLA, Los Angeles, California 90095

Damini Dey[f)]
Biomedical Imaging Research Institute, Department of Biomedical Sciences, Cedars Sinai Medical Center, Los Angeles, California 90048 and Department of Medicine, David-Geffen School of Medicine at UCLA, Los Angeles, California 90095

(Received 28 October 2014; revised 1 July 2015; accepted for publication 14 July 2015; published 5 August 2015)

Purpose: The authors aimed to develop and validate an automated algorithm for epicardial fat volume (EFV) quantification from noncontrast CT.
Methods: The authors developed a hybrid algorithm based on initial segmentation with a multiple-patient CT atlas, followed by automated pericardium delineation using geodesic active contours. A coregistered segmented CT atlas was created from manually segmented CT data and stored offline. The heart and pericardium in test CT data are first initialized by image registration to the CT atlas. The pericardium is then detected by a knowledge-based algorithm, which extracts only the membrane representing the pericardium. From its initial atlas position, the pericardium is modeled by geodesic active contours, which iteratively deform and lock onto the detected pericardium. EFV is automatically computed using standard fat attenuation range.
Results: The authors applied their algorithm on 50 patients undergoing routine coronary calcium assessment by CT. Measurement time was 60 s per-patient. EFV quantified by the algorithm (83.60 ± 32.89 cm^3) and expert readers (81.85 ± 34.28 cm^3) showed excellent correlation ($r = 0.97$, $p < 0.0001$), with no significant differences by comparison of individual data points ($p = 0.15$). Voxel overlap by Dice coefficient between the algorithm and expert readers was 0.92 (range 0.88–0.95). The mean surface distance and Hausdorff distance in millimeter between manually drawn contours and the automatically obtained contours were 0.6 ± 0.9 mm and 3.9 ± 1.7 mm, respectively. Mean difference between the algorithm and experts was $9.7\% \pm 7.4\%$, similar to interobserver variability between 2 readers ($8.0\% \pm 5.3\%$, $p = 0.3$).
Conclusions: The authors' novel automated method based on atlas-initialized active contours accurately and rapidly quantifies EFV from noncontrast CT. © *2015 American Association of Physicists in Medicine.* [http://dx.doi.org/10.1118/1.4927375]

Key words: epicardial fat, atlas-based segmentation, registration, active contours, line detection, noncontrast CT

1. INTRODUCTION

Epicardial fat is a particular depot of visceral fat around the heart, which is enclosed by the visceral pericardial sac.[1] Recent studies have shown a correlation between epicardial fat volume (EFV) and various manifestations of coronary artery disease, including adverse cardiovascular events,[2–4] myocardial ischemia,[5,6] coronary artery stenosis,[7,8] adverse plaque characteristics,[9–11] metabolic syndrome,[12] and atrial fibrillation.[13,14] Since epicardial fat is emerging as an important factor for cardiovascular risk stratification, it would be desirable to be able to accurately and noninvasively quantify it for a given patient in clinical practice. Epicardial fat can be visualized in noncontrast cardiac CT performed for assessment of coronary calcium, which is a low-cost, noninvasive scan with a low radiation burden.[15] However, epicardial fat is not assessed in

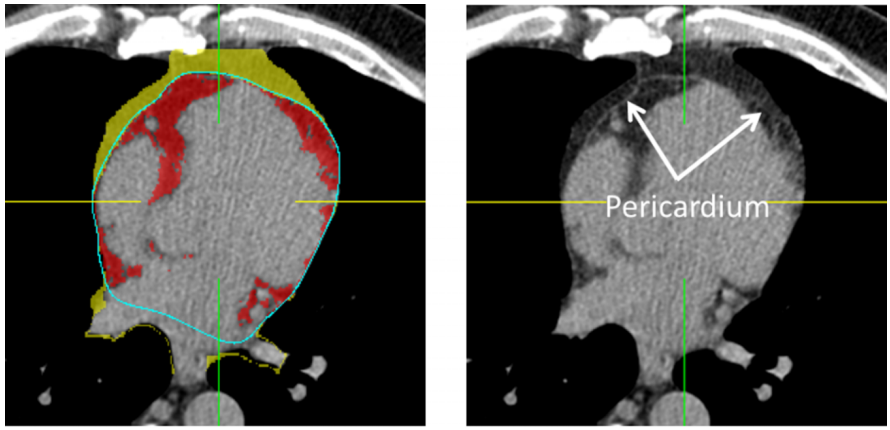

FIG. 1. (a) Epicardial fat (red, closest to the heart within the pericardium), thoracic fat (red and yellow, fat around the heart - which includes epicardial and extra-pericardial fat). (b) Pericardium indicated by arrows.

routine clinical practice, primarily due to the absence of a robust, automated quantification algorithm.

As illustrated in Fig. 1(a), epicardial fat (red) is the part of the thoracic fat (red and yellow) enclosed by the pericardium which is a tough double layered membrane that covers the heart. Epicardial fat is inside the pericardium and surrounds the coronary arteries directly, which makes it more correlated with coronary artery disease and thus has higher predictive value for cardiovascular risk stratification than thoracic fat which includes less related fat tissue outside the pericardium. There are two layers of the pericardial sac: the outermost fibrous pericardium and the inner serous pericardium. On noncontrast CT scans, the fibrous pericardium is identified as a thin curvilinear line of soft tissue density, well seen anterior to the right ventricle and in front of the right atrioventricular groove, where it is bordered by mediastinal and subepicardial fat of negative densities [Fig. 1(b)]. It is less often visible lateral to the left ventricle and in front of the interventricular groove. Pericardium is often not fully visible in CT images, which makes the detection of the boundaries of epicardial fat difficult. Thus, automated quantification of epicardial fat volume is particularly challenging since it requires identification of the pericardium, in addition to the thoracic cavity, and the heart.

Several investigators have reported methods for the quantification of only thoracic fat but not for the epicardial fat. Dey *et al.*[16] investigated semiautomated thoracic fat quantification from noncontrast CT. In this work, the lungs were first segmented by anterior sampling and adaptive threshold region-growing, followed by delineation of the inner contours of the thoracic cavity and determination of the cardiac bounding box. Yalamanchili *et al.*[17] described a thoracic fat quantification algorithm that used a classification-based method to discriminate fat from other tissues. The tissue classifier was constructed with three binary support vector machine (SVM) classifiers which are trained separately for different tissues (fat, muscle/blood, calcium). This method achieved an average overlap rate of 78% with expert annotations. Isgum *et al.*[18] have recently presented a multiatlas-based automated method for segmenting the heart, but not the pericardium for the purposes of coronary calcium quantification.

In several recent studies of epicardial fat, the pericardium has been traced manually by expert readers, which is time-consuming, requiring 7–10 min/patient.[1–6]

In the present study, we propose an automated algorithm for the measurement of EFV from noncontrast CT, which is based on a combination of registrations to multiatlas and geodesic active contours. This approach strictly follows the anatomic definition of the epicardial fat by local delineation of its boundaries (pericardium) with active contours, while preserving robustness by acquiring the global location and shape of the object from multiatlas. To validate the new algorithm, we compare its performance to that of experienced clinical readers.

2. OUR APPROACH

In this section, we present detailed description of the individual steps, including multiatlas segmentation method for the initial segmentation of the heart region and pericardium, pericardium detection, followed by geodesic active contours deformation.

Figure 2 shows the main steps of the algorithm. A noncontrast CT atlas (multiatlas) is first created from multiple coregistered noncontrast CT datasets in which the cardiac region and pericardium are manually segmented. Then, the global location and shape of the pericardium are initialized by combination of multiple registrations and label propagation from the multiatlas to the test noncontrast CT data [Fig. 2(b)]. Subsequently, the pericardium detection process [Fig. 2(c)] identifies the candidates for pericardial voxels, In the next step, the initial multiatlas boundaries are deformed by the geodesic active contours,[19] which are driven by the pericardium

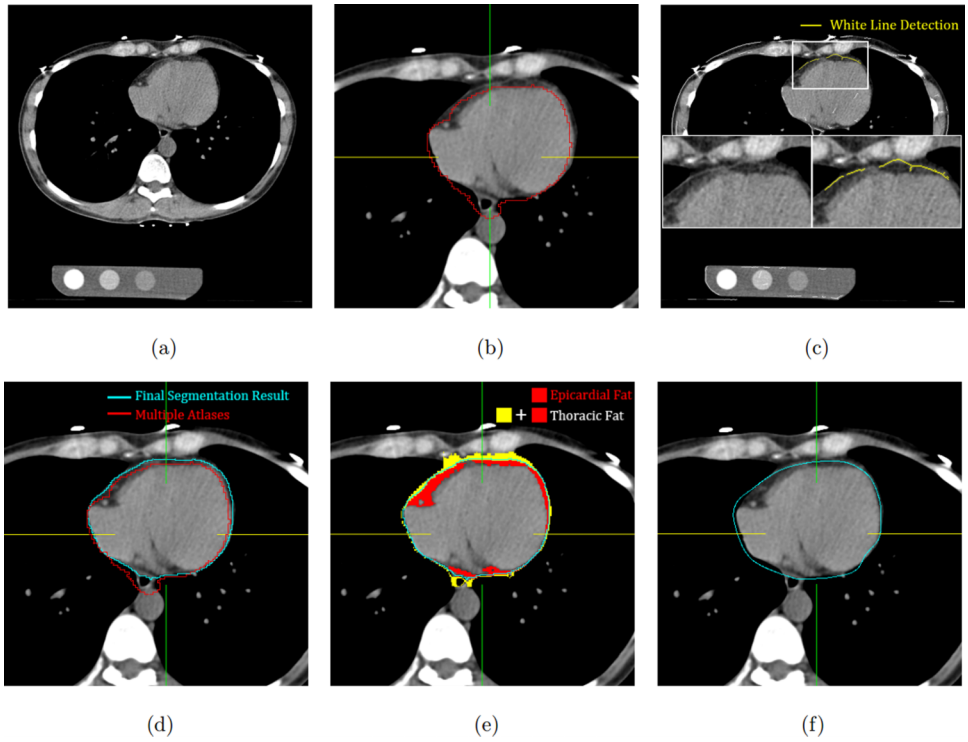

FIG. 2. Main steps of the algorithm (a) input image (3D volume), (b) rough location of pericardium obtained from multiple co-registered atlases (contour), (c) pericardium detection, (d) the multi-atlas initialization (red, contour below pericardium) and refined pericardium segmentation (blue, contour on pericardium), (e) epicardial fat quantification, (f) expert manual tracing shown for comparison.

detection results [Fig. 2(d)]. Finally, the volume of the epicardial fat is computed [Fig. 2(e)] within the pericardial sac boundaries using preset fat attenuation thresholds.[16]

2.A. Multiatlas segmentation

The multiatlas segmentation determines the initial location and shape of the heart and pericardium. The atlas was created from multiple patient scans ($N = 10$; 5 men and 5 women). For the atlas creation, on all transverse slices, 2D pericardial contours were manually traced by an expert cardiologist physician within the superior and inferior limits of the heart (Fig. 3). A 3D binary volume mask was generated from the 2D contours. Both atlas creation (Fig. 4) and target image segmentation are achieved by image registration. The nonlinear registration required for the atlas creation is computationally expensive. For the purpose of initial rough heart region segmentation, we accelerated the registration process by coregistering all the atlas images to a randomly selected primary atlas image with high image quality (low noise and no motion artifacts), as chosen by an expert radiologist. During segmentation of test patient data, only one transformation is computed between the primary atlas image and the patient image. This transformation is then applied to all the images in the atlas. This approach requires only one registration, with possibly lower segmentation accuracy.

The rigid and nonrigid registration problem is formulated as an optimization problem with respect to combined affine and B-spline transformations μ minimizing the difference between the target images and the reference image,

$$\widehat{\mu} = \arg\min_{\mu} C[\mu; U(\mathbf{p}), A(\mathbf{p})], \tag{1}$$

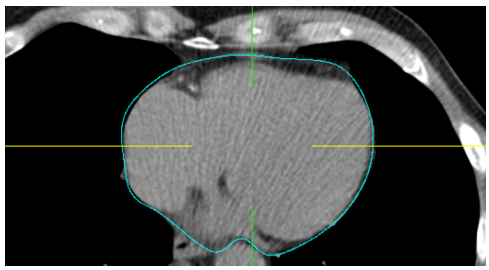

FIG. 3. An example of manually segmented contour on an atlas image.

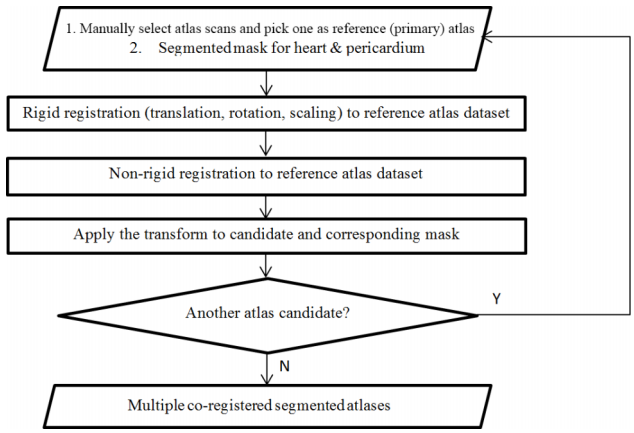

FIG. 4. Flowchart of the atlas creation procedure.

where $\widehat{\mu}$ is the transformation aligning atlas $A(\mu(\mathbf{p}))$ to target image $U(\mathbf{p})$, $\mathbf{p}$ denotes a voxel, and C is the negative mutual information.[20]

To obtain the rough binary segmentation of the pericardium $S(\mathbf{p})$, the labels S_i are propagated to the test image according to spatially varying decision fusion weights[18] that define the contribution of each atlas by measuring the similarity between the transformed moving atlas after registration and the target image. The similarity is measured by the absolute difference D_i between the transformed moving atlas and the target image,

$$D_i(\mathbf{p}) = |A_i(\mu(\mathbf{p})) - U(\mathbf{p})|, \forall i. \tag{2}$$

To determine how much a propagated label in each atlas image should contribute to the segmentation, weights λ_i were calculated as follows:

$$\lambda_i(\mathbf{p}) = \frac{1}{D_i(\mathbf{p}) \times g_{\sigma_1}(\mathbf{p}) + \epsilon}, \tag{3}$$

where $g_{\sigma_1}(\mathbf{p})$ is a Gaussian kernel of scale sigma that smooths the local estimate of the registration and ϵ is a small value to avoid division by zero. The resulting propagation label is determined by a weighted average of the transformed binary segmentation $S_i(\mu)$,

$$S(\mathbf{p}) = \frac{1}{\sum_{i=1}^{N} \lambda_i(\mathbf{p})} \sum_{i=1}^{N} \lambda_i(\mathbf{p}) S_i(\mu_i(\mathbf{p})). \tag{4}$$

2.B. Pericardium detection

To accurately localize the pericardium in the test image, $S(\mathbf{p})$ is transformed to a geodesic active contour model[19] driven by image features that indicate where the active contours should stop evolving. However, a traditional line detection responds to all edge structures[21] such as boundaries of the myocardium, edges between the heart and lungs, and outlines of the spine, but it does not respond sufficiently to the poorly visualized pericardium (Fig. 5). In a study of 260 patients by Delille *et al.*,[22] the maximal thickness of the normal pericardium was 2 mm for 95% of cases. Therefore, the width of the pericardium on the image in unit of pixel can be calculated by the physical thickness of the pericardium divided by the physical size of the pixel. For instance, for our image data, which have a physical pixel size of 0.68×0.68 mm^2 on each transverse slices, we can calculate the maximal width of pericardium in pixel by 2 mm/(0.68 mm/pixel) $\approx$ 3 pixels. As a result, we can set constant values to the width parameter in the pericardium detector described below. We have designed a feature detector that responds only to the pericardium, based on recent work in this area.[21] By examining the convolution response of a first-order derivative of Gaussian (DOG) to the signal with the cross section of a bright line, a dark line, and edge, respectively, we found that the DOG response can distinguish these three patterns. As a result, we can extract only the center of the bright lines by filtering out other patterns in the convolution response using

$$\mathrm{EP}(x,y) = \begin{cases} r(x-d,y) + |r(x+d,y)|, & r(x-d,y) > 0 \text{ and } r(x+d,y) < 0, \\ 0, & \text{otherwise.} \end{cases} \tag{5}$$

In Eq. (5), d is the half-width of the line to be detected, $r(x,y) = \left(-x/\sqrt{2\pi}\sigma_2^3\right)\left(e^{-(x^2/2\sigma_2^2)}\right) \times I(x,y)$ for $|x| \le 3\sigma_2, |y| \le L/2$, σ_2 is the standard deviation of the Gaussian function, and L is the length of the filter in the y direction. A fixed value of d can be used for pericardium detection because the width of the pericardium does not vary much across different subjects.[22] The response is then double thresholded[23] to obtain the centerline of the pericardium $T(\mathrm{EP}(x,y))$, as shown in Fig. 5(h). The pericardium detection result is then used as the external image-dependent force in the stopping function of the level-set geodesic flow. The stopping function $g(I)$ is defined as

$$g(I) = \frac{1}{1 + |T(\mathrm{EP}(x,y)) + \nabla I|}, \tag{6}$$

which is responsible for stopping the contour at the pericardium without interference from other anatomical structures. In the above stopping function, $T(\mathrm{EP}(x,y))$ is the detected pericardium centerline and ∇I is the gradient of the test image. The active contours can then lock onto the pericardium under the guidance of our stopping function after several iterations (<200 in our experiments) of evolving. We also implemented gradient vector flow (GVF) snake,[24] after initial atlas-based segmentation, to compare against our geodesic active contour method. We used gradient vector flow generated from the gradient image and pericardium detection on each transverse slice to direct the deformation of the snake. After the segmentation of the pericardium, a previously established threshold of −190 to −30 CT units (i.e., Hounsfield units)[12] is applied to fat-containing voxels within pericardial sac. This is the standard attenuation range for adipose tissue in noncontrast CT and has been validated by previous investigators.[12,25–29] Using the same threshold range, very good interscanner reproducibility for quantification of epicardial fat volume has been shown by Nakazato *et al.*, in 23 patients.[30] The fat tissue voxels are then summed to provide epicardial fat volume in milliliters. Figure 6 summarizes the whole automatic quantification process.

2.C. Analysis of algorithm performance

Pearson's correlation, Bland–Altman comparison, and the paired t-test were used to compare the volume enclosed by the pericardium obtained by our algorithm to the ground truth

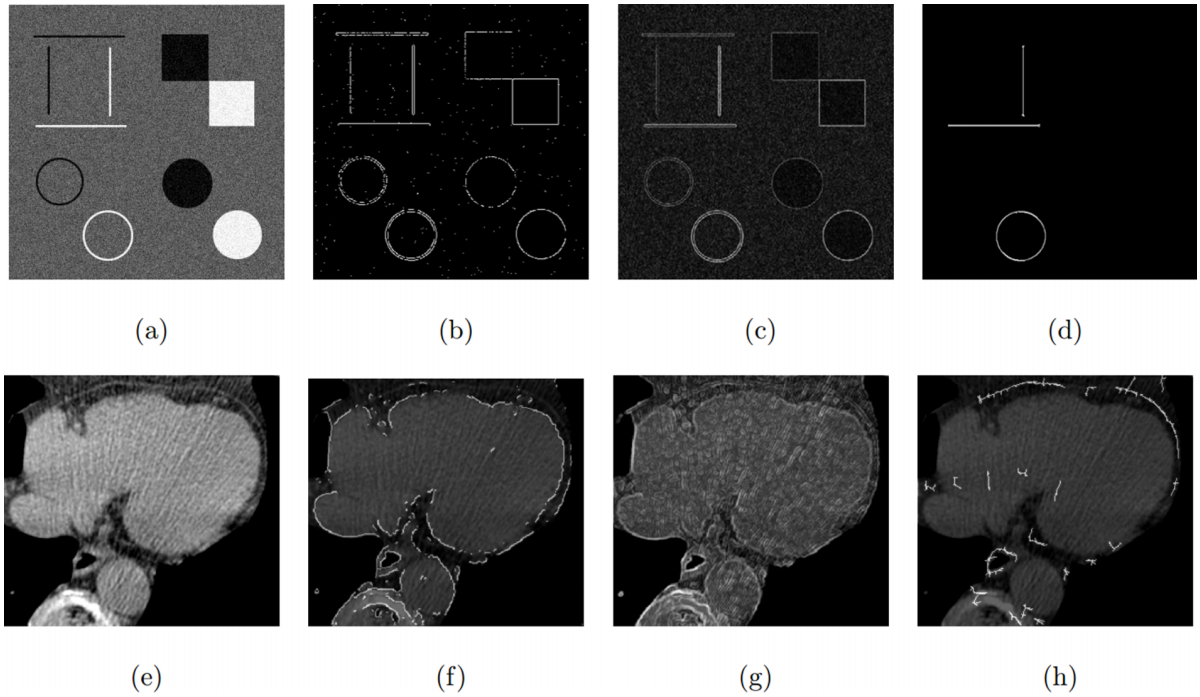

FIG. 5. Comparison of edge/line detection methods: [(a) and (e)] input synthetic and cardiac CT images, [(b) and (f)] Canny edge detection results: respond to edges between any objects with different intensities. [(c) and (g)] Gradient vector values: respond to intensity change in any directions, especially the boundary of the heart. [(d) and (h)] Our pericardium detection result: respond mostly to the pericardial sac.

determined by expert manual quantification. The overall Dice coefficient was used to measure the voxel overlap rate between them. We also calculated ten individual local Dice coefficients that describe the performance of our algorithm on different parts of the heart. To demonstrate that the pericardium detection and active contours deformation algorithms greatly improved the accuracy of the quantification results, we provided the results calculated without the above two methods.

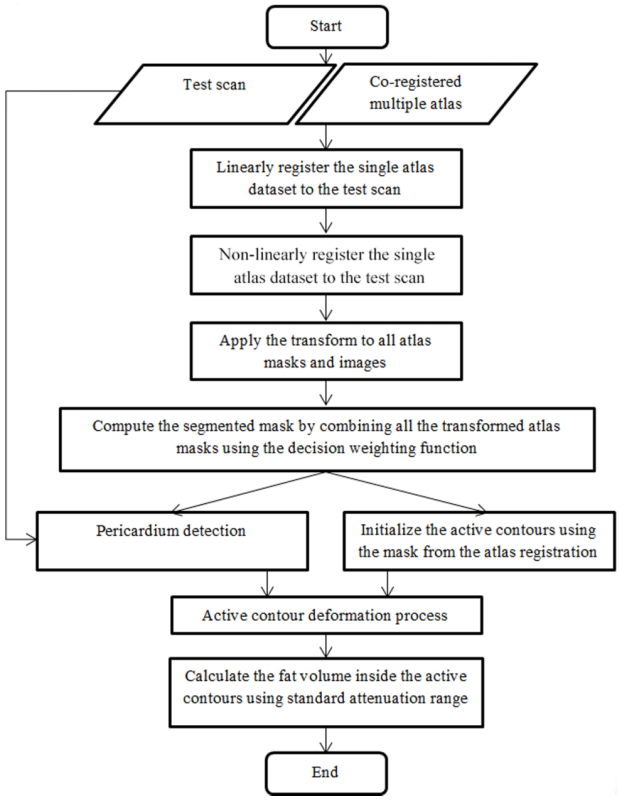

FIG. 6. The overall flowchart of the algorithm.

3. EXPERIMENTAL RESULTS

3.A. Image data

We analyzed consecutive noncontrast CT data collected for the routine assessment of coronary calcium, at the Cedars-Sinai Medical Center. Institutional Review Board (IRB) authorization for retrospective analysis and patient consent for such retrospective analysis was obtained in all cases. The CT images were acquired on a 4-slice multislice CT scanner (Siemens VolumeZoom) or an electron beam CT scanner (GE Imatron e-Speed) using a standard prospectively ECG-triggered imaging protocol for coronary calcium scoring.[31] Each CT dataset comprised 50–60 image slices with a space resolution of 512×512 pixels of size 0.68×0.68 mm^2 and a slice thickness of 2.5–3.0 mm. The datasets were selected from consecutive, asymptomatic patients undergoing standard coronary calcium scoring, and they were free of motion artifacts.

3.B. Parameter settings

By analyzing the properties of the image and searching in the parameter space, the best results were obtained with the following parameter setting. In multiple coregistered atlas segmentation, multiresolution approach was used (first with matrix size of 256 and then full-resolution 512 matrix)

for both affine and nonrigid B-spline registrations, in each of which 512 iterations of the stochastic gradient descent optimizer were performed. To estimate the derivative of the mutual information, 4096 image samples were used; they were randomly chosen for every iteration. For both affine and nonrigid registrations, 32 histogram bins were used. Gaussian smoothing with $\sigma_1 = 2$ voxels was performed on the difference image D_i before determining the weights for decision fusion. In pericardium detection, the filter [Eq. (5)] used $d = 3$ voxels as the half-width of the line to be detected, $L = 12$ voxels as the length of the filter in the y-direction, and $\sigma_2 = 2$ voxels which is the standard deviation of the Gaussian function. In geodesic active contour segmentation, the propagation scaling is 0.6, curvature scaling is 3.0, advection scaling is 1.0, maximum RMS error is 0.02, and number of iterations on each slice is 500. The gradient vector flow snake requires two parameters, which are used to generate the gradient vector flow external force field to drive the snake algorithm: the number of iterations (200) and the noise level of the input image (2000.0).

3.C. Results

Our algorithm was applied to 50 CT datasets described above. To compare the automatic quantification results with expert manual delineation, two experienced cardiac imaging readers, using consensus reading, manually traced the pericardium for all patient datasets. The time required for each expert to perform these tracings was about 10 min/case.

Epicardial fat volume for the 50 test datasets was 83.60 $\pm$ 32.89 cm^3 as measured by our automated algorithm and 81.85 $\pm$ 34.28 cm^3 according to the expert manual quantification, with no significant difference by comparison of individual data points ($p = 0.15$). The Bland–Altman plot [Fig. 7(a)] showed a positive bias of 1.75 cm^3 and the 95% limits of agreement ranged from −18.43 to 14.91 cm^3 with 49 out of the 50 test cases within the limits of 2 standard deviations. The algorithm quantification results were in excellent correlation ($R = 0.97$, $p < 0.0001$) with the ground truth measurements (Fig. 8). The mean Dice coefficient was 0.92 (range 0.88–0.95). The mean surface distance and Hausdorff distance in millimeter between manually drawn contours and the automatically obtained contours were 0.6 $\pm$ 0.9 mm and 3.9 $\pm$ 1.7 mm, respectively. Mean percentage difference between the algorithm and experts was 9.7% $\pm$ 7.4%, similar to the interobserver variability between 2 readers (8.0% $\pm$ 5.3%, $p = 0.3$).

In another experiment performed on the same dataset, we disabled the pericardium detection and geodesic active contours deformation process in our algorithm to show that these two steps improved the performance of our previous atlas-based method[32] significantly. Without pericardium detection and geodesic active contours deformation process, epicardial fat volume was underestimated as 63.55 $\pm$ 29.17 cm^3 which was significantly different from the expert manual quantification results ($p < 0.0001$). The Bland–Altman [Fig. 7(b)] showed a large negative bias of −19.61 cm^3 and 95% limits of agreement ranged from −49.49 to 12.89 cm^3 which was wider than that of the proposed method. The quantified volume by atlas had a lower correlation ($R = 0.89$, $p < 0.0001$) with the expert results. The average Dice coefficient was 0.88 (range 0.74–0.91). The mean surface distance and Hausdorff distance in millimeter were 1.0 $\pm$ 1.1 mm and 5.5 $\pm$ 2.7 mm, respectively, which were both significantly different from the results from our hybrid algorithm ($p < 0.0001$). Mean percentage difference between the atlas-only algorithm and experts was 26.5% $\pm$ 15.9% which was significantly larger than our proposed method ($p < 0.0001$) and the interobserver difference ($p < 0.0001$). A multiatlas segmentation method, weighted decision fusion with atlas selection (WDFS),[18] has been proved effective for cardiac and aortic segmentation. We implemented and compared this method with our hybrid approach. The results are detailed in Table I. To summarize, the performance of WDFS method on our 50 test cases using current 10 patient atlas images was lower than our proposed hybrid method and slightly higher than "multiatlas only"

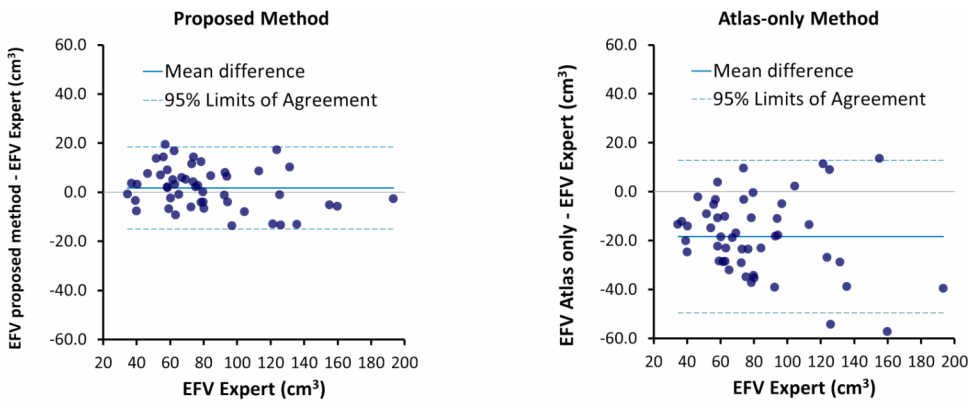

(a) (b)

FIG. 7. Bland–Altman plot for epicardial fat quantification (comparison between the performances with/without pericardium detection and geodesic active contours deformation). (a) The proposed algorithm: the bias was +1.75 cm^3 and the 95% limits of agreement ranged from −18.43 to 14.91 cm^3. (b) Use multiatlas initial segmentation only: the bias was −19.61 cm^3 and 95% limits of agreement ranged from −49.49 to 12.89 cm^3.

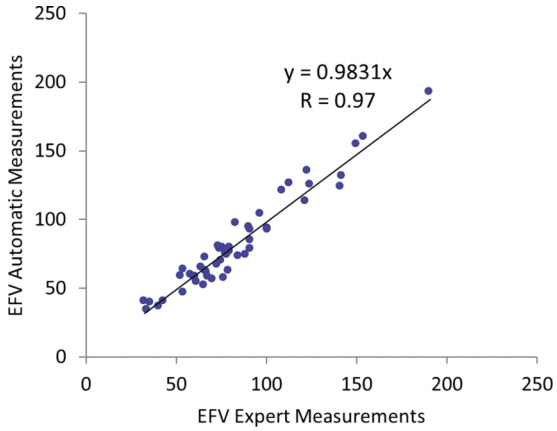

FIG. 8. Correlation between our algorithm and expert measurements.

method. The computation time was increased and proportional to the number of registrations performed.

In the experiment testing whether GVF snakes[24] can better handle complex anatomic structure in the superior and inferior sections of the heart, we replaced geodesic active contours with GVF snakes in our algorithm. With GVF snakes, epicardial fat volume was estimated as 69.89 ± 37.48 cm^3 which was significantly lower compared to the expert manual quantification results ($p < 0.0001$). While the correlation was high ($R = 0.94$, $p < 0.0001$) for this method, the bias was -11.96 cm^3 and 95% limits of agreement ranged from -37.19 to 13.27 cm^3 which was wider than that of the proposed method. The average Dice coefficient was 0.88 (range 0.72–0.95). The mean surface distance and Hausdorff distance in millimeter were 1.0 ± 0.8 mm and 5.6 ± 2.7 mm, respectively, which are both significantly different from the results from our hybrid method ($p < 0.01$, $p < 0.0001$). Percentage difference from the experts was slightly higher than that of our hybrid method. Therefore, the overall performance of GVF snake is slightly worse than that of the currently utilized method.

To illustrate the performance of the proposed algorithm in individual cases, we show three examples of our fat quantification results. Two of them (Figs. 9 and 10) were obtained from the 49 cases within the gray zone in the Bland–Altman plot (Fig. 8) and the third one is the largest outlier (Fig. 11) on which the algorithm had the worst performance. The Dice coefficient of the three cases was 0.9168 in Fig. 9, 0.9453 in Fig. 10, and 0.8806 in Fig. 11. In each figure, automatic epicardial fat segmentation results are in the first row and expert tracing of the pericardium is shown in the second row. As we can see from Figs. 9 and 10, the algorithm correctly detected the pericardium and segmented out the epicardial fat bounded by it. Figure 11 demonstrates the worst performance among the 50 test CT datasets. The contour which should overlap with the pericardium went beyond the imaged pericardium, which led to overestimation of the epicardial fat volume. In the superior section [Figs. 11(a) and 11(d)], the contour was overdeformed due to unsuccessful registration. Note also that some of the epicardial fat voxels are incorrectly identified in the middle of the heart due to the noisy data. We found that these CT data had minor reconstruction truncation artifacts compared with other normal coronary calcium score scans including those in our atlas. This was also a severely obese patient (body mass index (BMI) = 38 kg/m^2), which contributed to the big difference in the image appearance compared with the cases included in the atlas as well as noisy data due to severe photon attenuation in this patient. Significant difference between atlas images and target images, artifacts, and high image noise may cause unsuccessful rigid and nonrigid registration which can introduce incorrect initialization for the active contours. Even if the pericardium detector successfully identified the pericardium, the active contours will not evolve to lock onto it starting from a location far away from the pericardium. This restriction is needed to avoid the contours evolving to other objects when there is no visible pericardium. Most cases with obesity in our experiment had EFV accurately quantified. There were 9 cases out of 50 with BMI over 30 kg/m^2 (obese category). The mean difference of fat volume quantified for obesity group was $10.0\% \pm 12.3\%$ which was not significantly larger than the overall mean difference $9.7\% \pm 7.4\%$.

In Fig. 12, we measured the local Dice coefficient by grouping the transverse slices from superior to inferior into 10 regions and calculating Dice coefficient for each region separately. It can be seen that the algorithm works very well on the middle regions but loses some accuracy in the outside regions especially in the superior section. The

TABLE I. Performance comparison among the pure multiatlas-based method, WDFS method, multiatlas with GVF snakes, and proposed method.

	Multiatlas only	WDFS	Multiatlas and GVF snakes	Proposed method
EFV (cm^3)	63.55 ± 29.17[a,b]	69.08 ± 36.11[a,b]	69.89 ± 37.48[a,b]	83.60 ± 32.89[c]
Mean difference (%)	26.5 ± 15.9[b]	12.7 ± 10.3[b]	11.6 ± 9.6	9.7 ± 7.4
Bias (cm^3)	−19.61	−11.16	−11.96	1.75
95% LoA (cm^3)	−49.49 to 12.89	−41.28 to 15.73	−37.19 to 13.27	−18.43 to 14.91
Correlation (R)	0.89[b]	0.91[b]	0.94	0.97
Dice coefficient	0.88 (range 0.74–0.91)	0.89 (range 0.76–0.92)	0.88 (range 0.72–0.95)	0.92 (range 0.88–0.95)
Mean surface distance (mm)	1.0 ± 1.1[b]	1.0 ± 0.9[b]	1.0 ± 0.8[b]	0.6 ± 0.9
Hausdorff distance (mm)	5.5 ± 2.7[b]	5.1 ± 2.9[b]	5.6 ± 2.7[b]	3.9 ± 1.7

[a]Significantly different from expert results, $p < 0.0001$.
[b]Significantly different from the current proposed method, $p < 0.0001$.
[c]Not significantly different from expert results, $p = 0.15$.

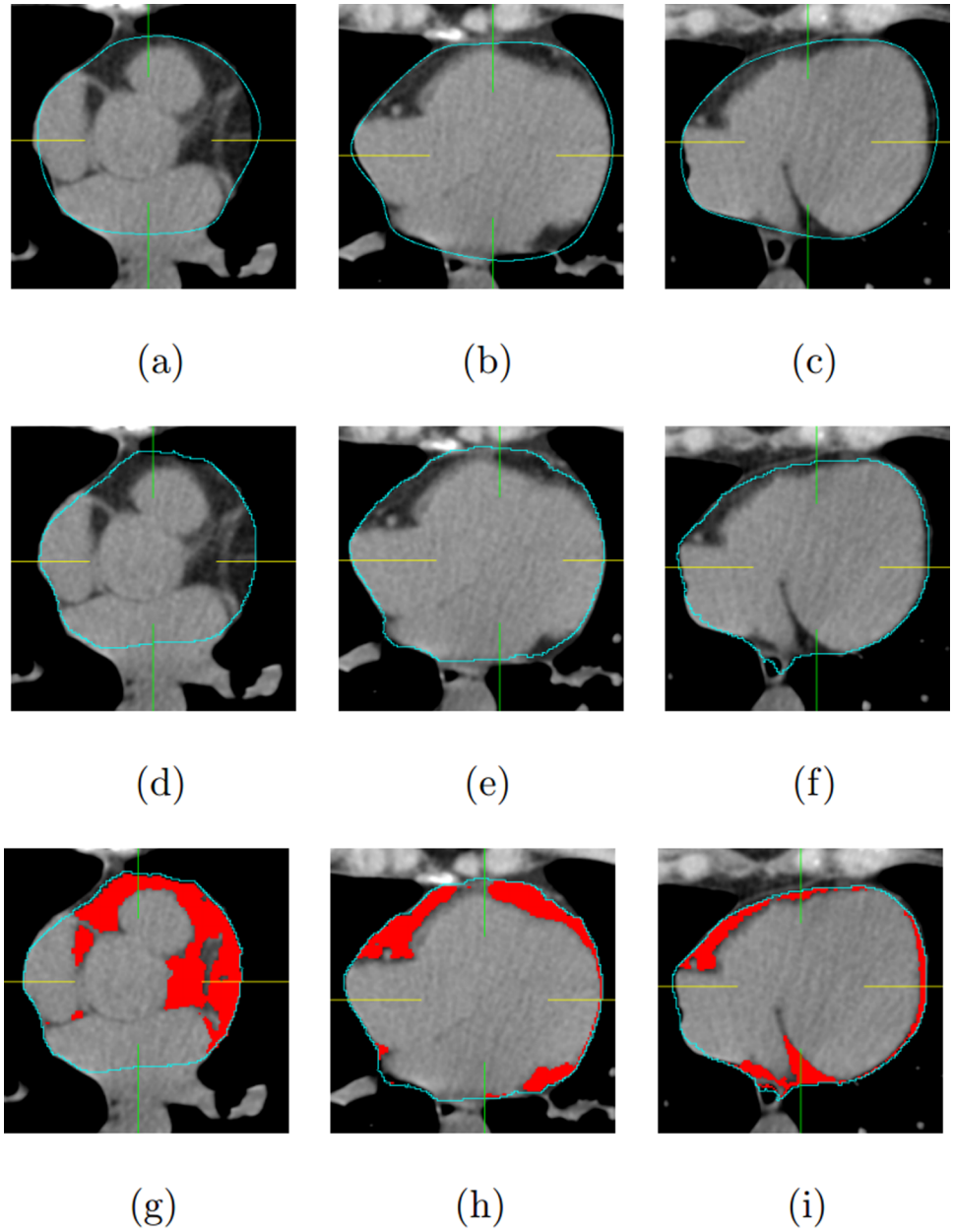

FIG. 9. Epicardial fat segmentation example with Dice coefficient 0.9168 and quantification results 60.2 cm^3 by the algorithm and 58.4 cm^3 by experts. (a)–(c) are expert pericardium tracing results on sample slices in superior section, middle section, and inferior section of the heart, respectively. (d)–(f) are the corresponding pericardium tracing results by our automated algorithm. (g)–(i) are automated epicardial fat segmentation results, in which epicardial fat (fat tissue close to heart within the pericardium) was labeled with mask.

complex anatomy in the superior section of the heart, where the pericardium is attached to aorta pulmonary veins and arteries, is a major contributor to this problem. There was also less agreement in the inferior sections. It should be also noted that in both superior and inferior sections there is increased operator variability in placement of the reference boundaries, which is likely contributing to the apparent lower segmentation accuracy. Additionally, the contours bounding the pericardium in the superior and inferior sections have much less area than those in the middle part. Thus, they do not contribute significantly to the overall Dice coefficient.

This performance was achieved in 60 s on a standard Windows PC (2.8 GHz CPU, 2GB RAM). On average, 11 s was used for rigid image registration, 24 s for nonrigid registration, and 25 s for the evolution of active contours.

4. DISCUSSION

Automated robust segmentation of subtle anatomical features in images is one of the biggest challenges in accurate epicardial fat quantification. Some work has been previously reported in this area. Figueiredo *et al.*[33] proposed a semiautomatic method for epicardial fat quantification. Their segmentation algorithm sweeps the anterior region from 0° to 180° registering the higher intensity point along each direction

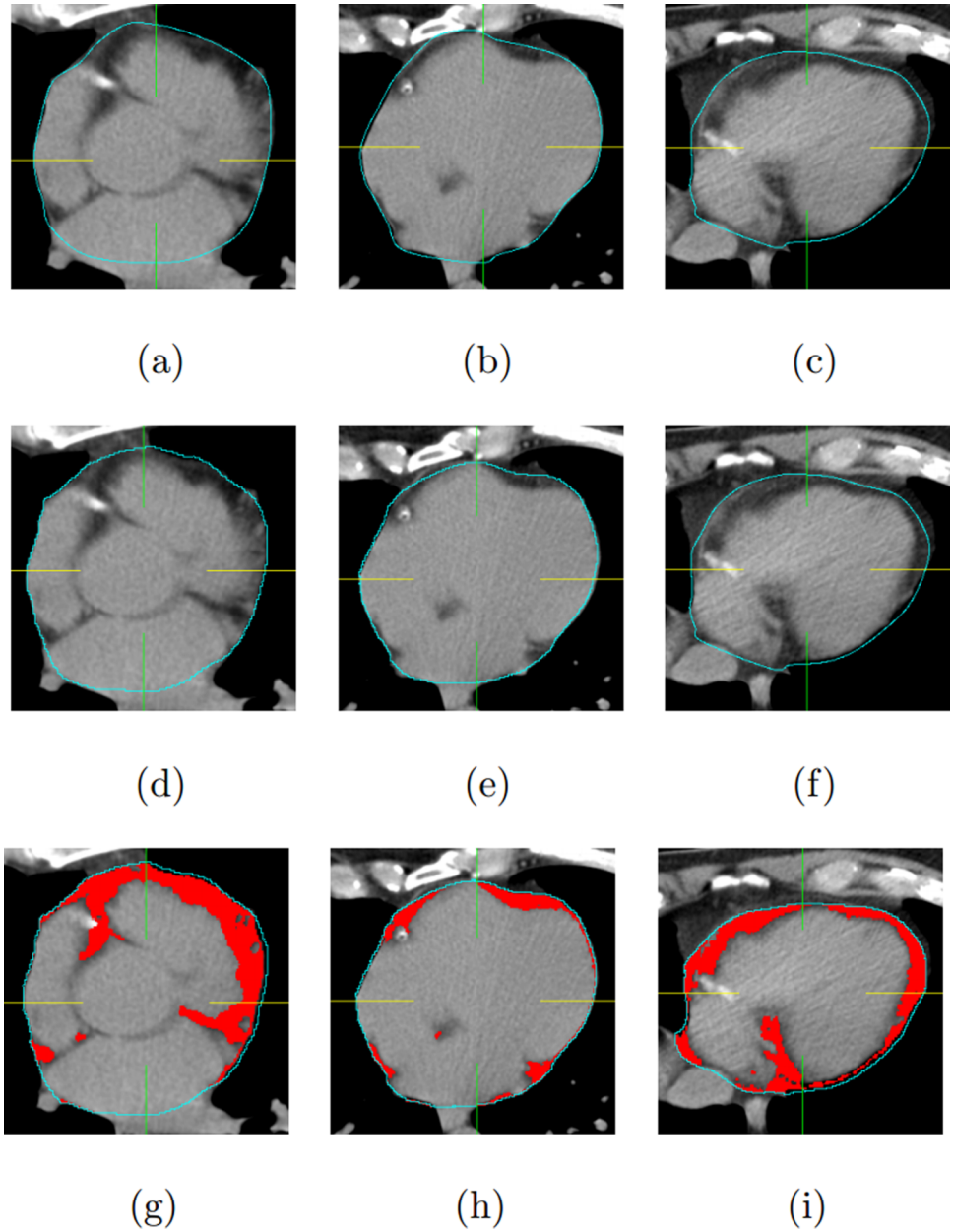

FIG. 10. Epicardial fat segmentation example with Dice coefficient 0.9453 and quantification results 91.4 cm^3 by the algorithm and 92.6 cm^3 by experts. (a)–(c) are expert pericardium tracing results on sample slices in superior section, middle section, and inferior section of the heart, respectively. (d)–(f) are the corresponding pericardium tracing results by our automated algorithm. (g)–(i) are automated epicardial fat segmentation results, in which epicardial fat (fat tissue close to heart within the pericardium) was labeled with mask.

to find control points belonging to the pericardium that appears in the image as a very thin line. In their method, users must manually set control points for spline interpolation in order to localize the pericardium line. Following this step, epicardial fat is quantified by considering only the pixels in the fat window of the CT image. Another semiautomatic method was proposed by Coppini *et al.*,[34] in which the task is separated into 2 steps. In the first step, an analysis of the epicardial fat intensity distribution is carried out in order to define suitable thresholds for a first rough segmentation. In the second step, a variational formulation of level set methods including a specially designed region homogeneity energy based on Gaussian mixture models is used to recover the spatial coherence and smoothness of fat deposits. This method also requires an expert observer to scroll the slices between the atrioventricular sulcus and the apex and to place control points on the pericardium. Shahzad *et al.*[35] proposed an automated epicardial fat quantification method using a multiatlas segmentation approach,[36] similar to the atlas-based initialization part in our method. The authors registered an atlas created with CTA data to the noncontrast test CT scans to segment the pericardium. In our study in a different population, we have shown (Sec. 3.B) by comparing to the multiatlas segmentation part of our algorithm that global registration of the heart region may not guarantee alignment of the pericardium, and the later two steps (pericardium detection

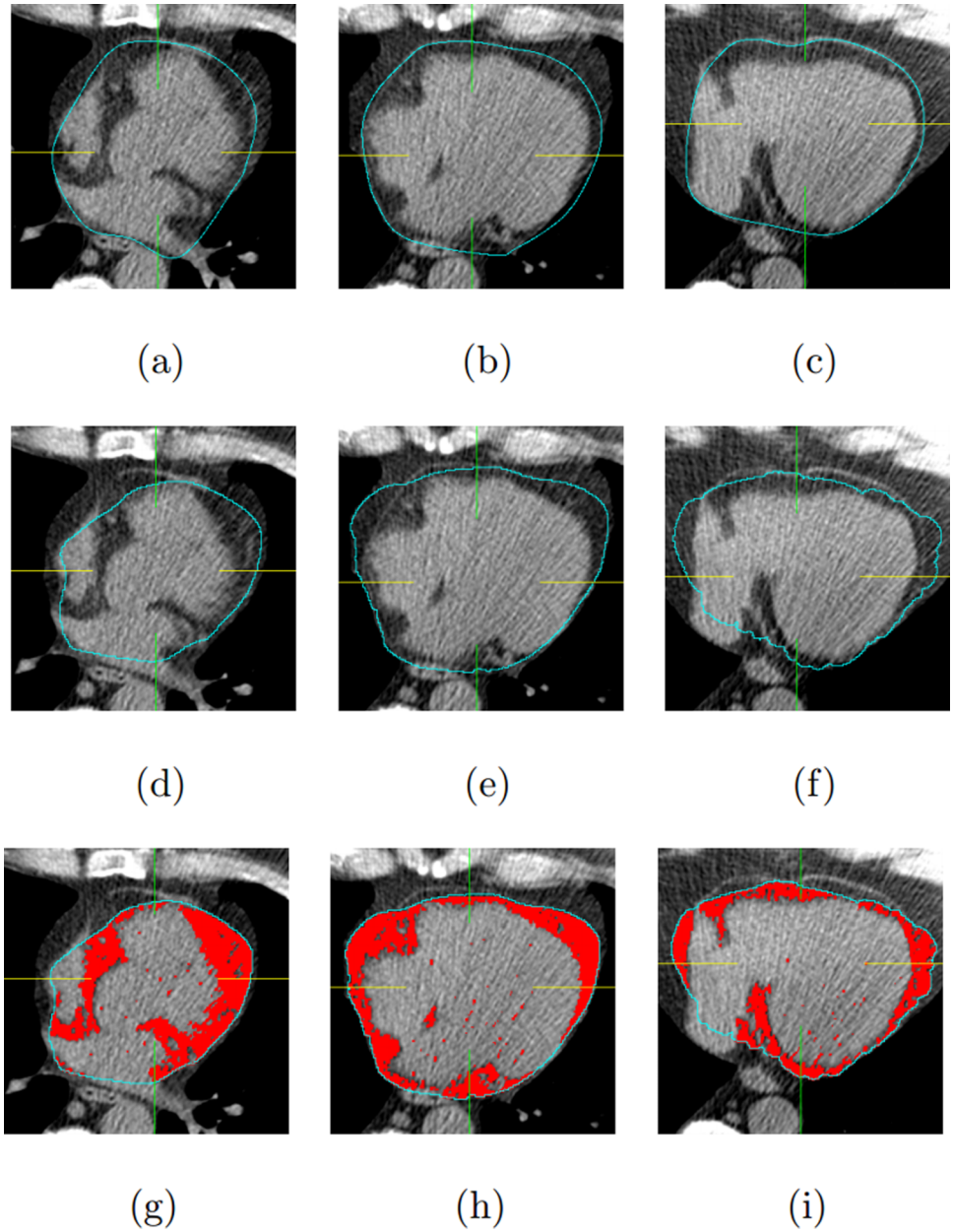

FIG. 11. Example of the worst performance on a patient with severe obesity (body mass index = 38 kg/m^2) with Dice coefficient 0.8806 and quantification results 180.7 cm^3 by the algorithm and 193.4 cm^3 by experts (a)–(c) are expert pericardium tracing results on sample slices in superior section, middle section, and inferior section of the heart, respectively. (d)–(f) are the corresponding pericardium tracing results by our automated algorithm. (g)–(i) are automated epicardial fat segmentation results, in which epicardial fat (fat tissue close to heart within the pericardium) was labeled with mask.

and active contours) significantly improve the performance. While we compared to consensus reading by two experts in our study, rather than to independent experts, we achieved slightly higher Dice coefficient (0.92 vs 0.89), higher correlation (0.97 vs 0.91), and lower bias (1.75 vs 16.6 cm^3), which could be the result of postatlas refinement of our algorithm. In their approach, volume registration is performed on each of the atlas cases to achieve EFV quantification in one subject, which may be computationally demanding.

In contrast to these previous methods, we have applied a knowledge-based thin membrane detection method to detect the visible part of the pericardium. In order to accurately lock the segmentation contours onto the pericardium, we used active contour model driven by the pericardium detection result supported by the robust localization of the inner thoracic cavity and pericardium with a fast multiatlas registration method. To lock the contour precisely to the pericardium, we initialize active contours from the atlas labels and drive it using a pericardium detector that extracts only the pericardium in the images. In addition, in our approach when the multiatlas is created, individual atlas scans are coregistered to a primary image in order to avoid a costly one-to-all registration for the test image. As a result, when segmenting a single test image, the time-consuming registration process is performed only once. Although the atlas-based segmentation result is sensitive to the registration error between the primary atlas

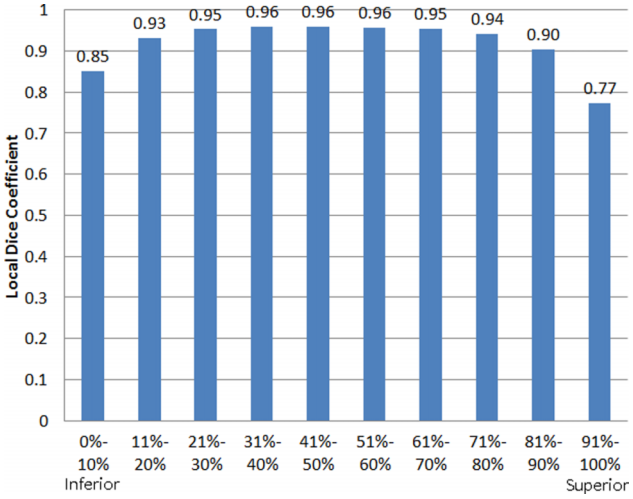

FIG. 12. Local Dice coefficient from inferior section to superior section.

and the patient data, we used coregistered atlas to restrict the computation time. In our study, the initial atlas-based alignment was visually assessed for each case in our study and was found to be correctly aligned. It is also useful to note that the coregistered atlas-based segmentation is only the rough initialization of the heart position and shape, not the final contour which is expected to be accurate. We have validated the effect of pericardium detection and active contours deformation process in increasing the accuracy of the algorithm by comparing the performance to our atlas-based method[32] and gradient vector flow snakes on the same datasets (see Sec. 3.B). With only the multiatlas segmentation, EFV was significantly underestimated, which caused lower correlation, dice overlap, and higher bias. The two Bland–Altman plots (Fig. 7) drawn under the same scale and Table I illustrate the improvements in performance. To our knowledge, ours is the first method to use such atlas-initialized active contours to segment subtle anatomical features such as the pericardium. The atlas incorporate prior information may be changed by users, which may allow our framework to be applicable to contrast-enhanced cardiac CT, particularly coronary CT angiography.

There are some limitations in our approach. The selection of cases used to create the atlas may affect the performance of the initial segmentation of the heart and pericardium, which is a common limitation among atlas-based methods. We randomly selected the primary atlas instead of performing leave-one-out or cross-validation analysis on the atlas sets which might result in better performance. Sufficient number and diversity in atlas cases may enable the algorithm to have better performance on a wider range of test data. Nevertheless, the use of the geodesic active contours as a second step in our algorithm should minimize this problem.

5. CONCLUSION

Our hybrid approach of atlas registration and active contour segmentation proves to be effective for the accurate delineation of subtle image features such as the pericardium, while it preserves the location and shape of the anatomical structure of interest. This method will allow physicians and researchers to quantify the epicardial fat volume in patients quickly, largely without minimal user intervention.

ACKNOWLEDGMENT

This study was supported by American Heart Association Grant No. 12GRNT9450056 (to Dr. Dey).

[a]Electronic mail: xiaowei@cs.ucla.edu.
[b]Electronic mail: dt@cs.ucla.edu.
[c]Electronic mail: diazzmariana@gmail.com
[d]Electronic mail: daniel.berman@cshs.org
[e]Electronic mail: piotr.slomka@cshs.org
[f]Electronic mail: damini.dey@cshs.org

[1]D. Dey, R. Nakazato, P. J. Slomka, and D. S. Berman, "CT quantification of epicardial fat: Implications for cardiovascular risk assessment," Curr. Cardiovasc. Imaging Rep. **5**, 352–359 (2012).
[2]V. Y. Cheng *et al.*, "Pericardial fat burden on ECG-gated noncontrast CT in asymptomatic patients who subsequently experience adverse cardiovascular events," JACC: Cardiovasc. Imaging **3**, 352–360 (2010).
[3]A. A. Mahabadi, J. M. Massaro, G. A. Rosito, D. Levy, J. M. Murabito, P. A. Wolf, C. J. O'Donnell, C. S. Fox, and U. Hoffmann, "Association of pericardial fat, intrathoracic fat, and visceral abdominal fat with cardiovascular disease burden: The framingham heart study," Eur. Heart J. **30**, 850–856 (2009).
[4]A. A. Mahabadi *et al.*, "Association of epicardial fat with cardiovascular risk factors and incident myocardial infarction in the general populationthe heinz nixdorf recall study," J. Am. Coll. Cardiol. **61**, 1388–1395 (2013).
[5]B. Tamarappoo *et al.*, "Increased pericardial fat volume measured from noncontrast CT predicts myocardial ischemia by SPECT," JACC: Cardiovasc. Imaging **3**, 1104–1112 (2010).
[6]M. Janik, G. Hartlage, N. Alexopoulos, Z. Mirzoyev, D. S. McLean, C. D. Arepalli, A. E. Stillman, and P. Raggi, "Epicardial adipose tissue volume and coronary artery calcium to predict myocardial ischemia on positron emission tomography-computed tomography studies," J. Nucl. Cardiol. **17**, 841–847 (2010).
[7]Y. Hirata *et al.*, "Coronary atherosclerosis is associated with macrophage polarization in epicardial adipose tissue," J. Am. Coll. Cardiol. **58**, 248–255 (2011).
[8]P. M. Gorter, A. M. de Vos, Y. van der Graaf, P. R. Stella, P. A. Doevendans, M. F. Meijs, M. Prokop, and F. L. Visseren, "Relation of epicardial and pericoronary fat to coronary atherosclerosis and coronary artery calcium in patients undergoing coronary angiography," Am. J. Cardiol. **102**, 380–385 (2008).
[9]M. Konishi *et al.*, "Association of pericardial fat accumulation rather than abdominal obesity with coronary atherosclerotic plaque formation in patients with suspected coronary artery disease," Atherosclerosis **209**, 573–578 (2010).
[10]N. Alexopoulos, D. S. McLean, M. Janik, C. D. Arepalli, A. E. Stillman, and P. Raggi, "Epicardial adipose tissue and coronary artery plaque characteristics," Atherosclerosis **210**, 150–154 (2010).
[11]R. Rajani *et al.*, "Relationship of epicardial fat volume to coronary plaque, severe coronary stenosis, and high-risk coronary plaque features assessed by coronary CT angiography," J. Cardiovasc. Comput. Tomogr. **7**, 125–132 (2013).
[12]D. Dey *et al.*, "Computer-aided non-contrast CT-based quantification of pericardial and thoracic fat and their associations with coronary calcium and metabolic syndrome," Atherosclerosis **209**, 136–141 (2010).
[13]M. O. Al Chekakie, C. C. Welles, R. Metoyer, A. Ibrahim, A. R. Shapira, J. Cytron, P. Santucci, D. J. Wilber, and J. G. Akar, "Pericardial fat is independently associated with human atrial fibrillation," J. Am. Coll. Cardiol. **56**, 784–788 (2010).
[14]C. X. Wong *et al.*, "Pericardial fat is associated with atrial fibrillation severity and ablation outcome," J. Am. Coll. Cardiol. **57**, 1745–1751 (2011).

[15]R. L. Morin, T. C. Gerber, and C. H. McCollough, "Radiation dose in computed tomography of the heart," Circulation **107**, 917–922 (2003).
[16]D. Dey, Y. Suzuki, S. Suzuki, M. Ohba, P. J. Slomka, D. Polk, L. J. Shaw, and D. S. Berman, "Automated quantitation of pericardiac fat from non-contrast CT," Invest. Radiol. **43**, 145–153 (2008).
[17]R. Yalamanchili, D. Dey, U. Kukure, R. Nakazato, D. S. Berman, and I. A. Kakadiaris, "Knowledge-based quantification of pericardial fat in non-contrast CT data," Proc. SPIE **7623**, 76231X (2010).
[18]I. Isgum, M. Staring, A. Rutten, M. Prokop, M. A. Viergever, and B. van Ginneken, "Multi-atlas-based segmentation with local decision fusion-application to cardiac and aortic segmentation in CT scans," IEEE Trans. Med. Imaging **28**, 1000–1010 (2009).
[19]V. Caselles, R. Kimmel, and G. Sapiro, "Geodesic active contours," Int. J. Comput. Vision **22**, 61–79 (1997).
[20]P. Thévenaz and M. Unser, "Optimization of mutual information for multiresolution image registration," IEEE Trans. Image Process. **9**, 2083–2099 (2000).
[21]L. Zhang *et al.*, "Dark line detection with line width extraction," in *15th IEEE International Conference on Image Processing, 2008. ICIP 2008* (IEEE, Piscataway, NJ, 2008), pp. 621–624.
[22]J. Delille, A. Hernigou, V. Sene, G. Chatellier, J. Boudeville, P. Challande, and M. Plainfosse, "Maximal thickness of the normal human pericardium assessed by electron-beam computed tomography," Eur. Radiol. **9**, 1183–1189 (1999).
[23]J. C. Russ, *The Image Processing Handbook* (CRC, Boca Raton, FL, 2010).
[24]C. Xu and J. L. Prince, "Snakes, shapes, and gradient vector flow," IEEE Trans. Image Process. **7**, 359–369 (1998).
[25]D. Dey, T. Schepis, M. Marwan, P. J. Slomka, D. S. Berman, and S. Achenbach, "Automated three-dimensional quantification of noncalcified coronary plaque from coronary CT angiography: Comparison with intravascular US 1," Radiology **257**, 516–522 (2010).
[26]G. L. Wheeler *et al.*, "Pericardial and visceral adipose tissues measured volumetrically with computed tomography are highly associated in type 2 diabetic families," Invest. Radiol. **40**, 97–101 (2005).
[27]T. Yoshizumi *et al.*, "Abdominal fat: Standardized technique for measurement at CT 1," Radiology **211**, 283–286 (1999).
[28]H. Kvist, B. Chowdhury, U. Grangård, U. Tylen, and L. Sjöström, "Total and visceral adipose-tissue volumes derived from measurements with computed tomography in adult men and women: Predictive equations," Am. J. Clin. Nutr. **48**, 1351–1361 (1988).
[29]L. Sjostrom, H. Kvist, A. Cederblad, and U. Tylen, "Determination of total adipose tissue and body fat in women by computed tomography, 40k, and tritium," Am. J. Physiol.: Endocrinol. Metab. **250**, E736–E745 (1986).
[30]R. Nakazato, H. Shmilovich, B. K. Tamarappoo, V. Y. Cheng, P. J. Slomka, D. S. Berman, and D. Dey, "Interscan reproducibility of computer-aided epicardial and thoracic fat measurement from noncontrast cardiac CT," J. Cardiovasc. Comput. Tomogr. **5**, 172–179 (2011).
[31]T. S. Polonsky, R. L. McClelland, N. W. Jorgensen, D. E. Bild, G. L. Burke, A. D. Guerci, and P. Greenland, "Coronary artery calcium score and risk classification for coronary heart disease prediction," JAMA, J. Am. Med. Assoc. **303**, 1610–1616 (2010).
[32]D. Dey, A. Ramesh, P. J. Slomka, R. Nakazato, V. Y. Cheng, G. Germano, and D. S. Berman, "Automated algorithm for atlas-based segmentation of the heart and pericardium from non-contrast CT," Proc. SPIE **7623**, 762337 (2010).
[33]B. Figueiredo, J. G. Barbosa, N. Bettencourt, and J. M. R. Tavares, "Semi-automatic quantification of the epicardial fat in CT images," in *VipIMAGE 2009-II ECCOMAS Thematic Conference on Computational Vision and Medical Image Processing* (Taylor & Francis Group, Abingdon, 2009).
[34]G. Coppini, R. Favilla, P. Marraccini, D. Moroni, and G. Pieri, "Quantification of epicardial fat by cardiac CT imaging," Open Med. Inf. J. **4**, 126–135 (2010).
[35]R. Shahzad *et al.*, "Automatic quantification of epicardial fat volume on non-enhanced cardiac CT scans using a multi-atlas segmentation approach," Med. Phys. **40**, 091910 (9pp.) (2013).
[36]H. Kirişli *et al.*, "Evaluation of a multi-atlas based method for segmentation of cardiac CTA data: A large-scale, multicenter, and multivendor study," Med. Phys. **37**, 6279–6291 (2010).